Bio-Inspired Ag-MnO_2 Nanocomposite for Efficient Photodegradation of Orange G Dye and Antibacterial Applications

Rakesh Kumar Meena[1], Ashwini Singhal[1], Anita Kumari[1], Priyadarshi Meena [2] and Ramhari Meena[1]*
[1]*Department of Chemistry, University of Rajasthan, Jaipur, Rajasthan-302004, India*
[2]*Department of Zoology, University of Rajasthan, Jaipur, Rajasthan-302004, India*
*Corresponding authors: ramharichem@gmail.com, ramharimeena@uniraj.ac.in

Abstract

In the present study, *Lawsonia inermis L.* leaf extract was employed for the green synthesis of silver-doped manganese oxide nanocomposites (Ag–MnO_2 NCs). The synthesized nanocomposites were characterized using various physicochemical techniques, which confirmed good dispersion of silver particles over MnO_2 layers and an average particle size of ~16.21 nm, as revealed by TEM analysis. UV–Vis absorption spectra indicated enhanced visible light absorption in Ag–MnO_2 NCs compared to undoped counterparts. The photocatalytic activity of the nanocomposites was evaluated using Orange G (OG) dye under visible light irradiation, with systematic investigation of catalyst dose, initial dye concentration, and solution pH. Optimal conditions (20 mg/L OG dye at neutral pH) resulted in nearly 92% dye degradation within 90 minutes, following pseudo-first-order kinetics with an apparent rate constant of 0.01932 min^{-1}. In addition, the Ag–MnO_2 NCs displayed significant antibacterial activity against both Gram-positive (*Bacillus subtilis*, *Staphylococcus aureus*) and Gram-negative (*Escherichia coli*, *Pseudomonas aeruginosa*) strains, along with good stability in neutral aqueous media. These findings demonstrate the potential of green-synthesized Ag–MnO_2 NCs as efficient, eco-friendly photocatalysts and antibacterial agents for environmental and biomedical applications.

Keywords: Ag-MnO_2nanocomposite, Photodegradation, Orange G dye, Antibacterial properties

1. Introduction

Dyes are the coloured substances that are used to provide colour to textiles, culinary items, leather, wool, and other materials. Dyes are divided into several groups depending on their colour, structure, and intended use, for instance, anthraquinone, indigo, nitro, azo, and nitroso dyes [1]. Numerous industries, including the paper, food, and leather sectors, extensively employ dyes. These dyes are widely used in various industries, including the food, textile, paper, cosmetic, and pharmaceutical sectors, due to their wide range and affordability [2]. It is estimated that around 7×10^5 tonnes of dyes are produced annually, of which 10 to 15% are released during the coloring process. Many textile businesses utilise about 10,000 distinct types of dyes. The dye waste material is highly toxic and hazardous to both human health and the environment, as it contains several poisonous substances. As a result, amphibian bodies receive and emit a significant amount of dyed wastewater annually [3-4]. The release of dyed water into amphibian bodies from various industries reduces light saturation, which affects the process of photosynthesis. Skin issues like inflammation, allergies, and cancer-causing transformation are among the unfavourable effects on human health. In addition to producing cancer, dyes can have significant negative health consequences on humans, such as impairing the reproductive and neurological systems and causing brain and nervous system dysfunction. Therefore, the use of dyes has raised considerable concern due to their toxic effects [5].

Orange G dye is a member of the Azo dye class. It is the disodium salt of 7-hydroxy-8-[(E) phenyldiazenyl] naphthalene-1,3-disulfonic acid. One azo group is joined to an aromatic ring in the OG dye. The chemical formula for it is $C_{16}H_{10}N_2Na_2O_7S_2$. OG dye is widely used to dye materials, including leather, paper, wool, and fibre. Its unfavourable effects on human health include skin conditions such as allergies, skin irritation, and cancer-causing transformation. Wastewater from industry that contains too much orange G. OG dye requires treatment to protect the environment [6-7].

Nowadays, many current photocatalytic materials are made up of metal oxides such as TiO_2, SnO_2, ZnO, CuO, metal organic frameworks, and spinel ferrites. However, the effectiveness of binary oxide/sulfide photocatalysis remains low due to their high resistance, fast electron-hole pair recombination, unsuitable band gap, unstable nature, and photo-corrosion. The scientific community has faced many obstacles in the creation of an active semiconductor photocatalyst. Transition metal groups (MO_2) (M = Mn, Co, Ni, Cu, and Zn) are attracting the attention of research groups because of their remarkable stability, low cost, and distinctive crystal structure. Additionally, these materials have a wide range of applications across numerous scientific domains [8-9]. Manganese dioxide (MnO_2) is a transition metal oxide that exhibits exceptional reactivity, robustness, and a very efficient capacity to absorb visible light with a band gap between ~1 and 3.5 eV [10]. Furthermore, it has become more significant in the construction of sensors because of its distinct ionic, multi-ferroic, and electro-chromic properties. MnO_2 remains one of the materials with the highest potential for visible light-harvesting photocatalytic qualities because of its reduced band gap and effective sunlight-harvesting capabilities [11]. There is illustrative work that demonstrates the potential of magnetic silver nanoparticles, biosynthesised silver-impregnated cyclodextrin nanoparticles, and manganese dioxide doped with silver nanoparticles by green synthesis in water treatment. Applications for metal oxide nanoparticles are numerous and include sensors, antibacterial agents, photocatalysis, and lightweight materials. Environmental friendliness, recyclability, and reproducibility with simple methods are among the advantages of photocatalysts. However, the following factors should be considered while building a photocatalyst: its rate of charge recombination, response to a broad spectrum of light waves, and mechanical and optical stability. Photocatalysts currently present challenges for large-scale real-time applications due to their prohibitive cost, inferior performance, unstable defects, stiff internal geometry, and electronic energy band structure that is challenging to change over broad regions [12].

The production of NCs using an aqueous extract of *Lawsonia inermis L.* is described in this paper. This plant is well-known around the world for its use in temporary tattoos and as a therapeutic plant under the name of its derivative product, henna. The chemical composition of *Lawsonia inermis L.* was discovered through phytochemical studies, which include phenolic, tartaric, citric, anthraquinones, stilbenoids, polyphenols, triterpenes, carotenoids, naphthalene, and other components, such as hennosides, the glucosidic precursors of lawsonin, the dyeing ingredient [13-14]. Most of these components, particularly organic acids, have potent reducing properties. The goal of the work was to use leaf extract from *Lawsonia inermis L.*to synthesise silver-doped manganese oxide nanocomposite(Ag-MnO_2NCs), and investigate the photocatalytic activity using the OG dye degradation process. The antibacterial activity of the resultant Ag-MnO_2 NCs was evaluated after they were characterised using a variety of techniques, including TEM, FESEM, XRD, FTIR, and UV-Vis.

2. Materials and methods

2.1 Chemicals, reagents and plant Source

Fresh and healthy leaves of *Lawsonia inermis L.*, commonly known as henna, were meticulously harvested from a plant nursery at the University of Rajasthan in Jaipur, Rajasthan. For the synthesis of nanomaterials, a range of analytical-grade chemicals was procured from Sigma-Aldrich, including silver nitrate ($AgNO_3$) and potassium permanganate ($KMnO_4$). The Orange G dye was obtained from Hi-Media.All glassware is thoroughly cleaned and subsequently rinsed with double-distilled water prior to its use in the synthesis procedure.

2.2 Instrumentation

A Fourier transform infrared spectrometer (Bruker ALPHA) was utilized to capture FT-IR spectra within the 4000-500 cm^{-1} range, effectively confirming the diverse functional groups and bond types present in the biosynthesized nanocomposites (NCs). To assess the optical properties, UV-Vis absorption spectra were recorded from 200 to 800 nm using a Shimadzu UV-2600 spectrophotometer. To explore the crystal structure and determine the crystallite size of the biosynthesized NCs, we collected Powder X-ray diffraction (PXRD) patterns over a 2θ range of 5 to 90° using an X-ray diffractometer (Model: SMARTLAB). The surface morphology of the samples was examined using a Field Emission Scanning Electron Microscope (FESEM) from JEOL, specifically the JSM-7610F Plus model. Additionally, High-Resolution Transmission Electron Microscopy (HRTEM) images were obtained using the Tecnai G2 20 TWIN model.

2.3 Collection and preparation of leaf extract

Leaves of *L. inermis* were obtained from a plant nursery located at the University of Rajasthan in Jaipur, Rajasthan. The collected leaves were thoroughly washed with distilled water to remove any surface impurities. After cleaning, the leaves were shade-dried at room temperature and then cut into small pieces. The dried leaves were ground into a fine powder using a mortar and pestle. A total of 10 grams of this powder was mixed with 100 milliliters of distilled water heated to 80°C. This mixture was stirred for 30 minutes with a magnetic stirrer set to 200 rpm. The resulting plant extract was filtered twice using Whatman No. 1 filter paper and stored at 4°C for future use.

2.4 Biosynthesis of MnO_2-NPs and Ag-MnO_2 NCs

MnO_2-NPs and Ag-MnO_2 NCs were synthesised by using the *L. inermis L.* leaf extract.1 mM of $KMnO_4$ (7.90 mg) salt was added slowly into the 50 mL of *Lawsonia inermis L.* leaf extract for MnO_2 NPs synthesis under continuous stirring at pH 7, and then heated at a temperature of 80°C. For the synthesis of Ag-MnO_2 NCs, a mixture of 8.49 mg of $AgNO_3$ (1 mM) and 7.90 mg of $KMnO_4$ (1 mM) salts was added slowly into 50 mL of *Lawsonia inermis L.* leaf extract under continuous stirring at pH 7, and then heated and maintained at a temperature of 80°C during the reaction. Afterward, the product was washed with DI water until neutral pH and then rinsed twice using ethanol. Finally, the obtained MnO_2-NPs and Ag-MnO_2NCs were left to dry overnight at a temperature of 60°C [15-16].

2.5 Photocatalytic degradation ofOG dye

The photocatalytic performance of the biosynthesized nanomaterials was assessed by examining the degradation of Orange G dye under visible light using a custom-designed photoreactor equipped with a 250 W sodium vapor lamp. This study also examined the effects of various parameters on the photocatalytic performance, including catalyst loading and pH effect. A standard approach involved dispersing 60 mg of Ag-MnO2 NCs in 100 mL of OG solution (20 mg/L) to examine the impact of initial OG dye concentration on photocatalytic activity. To achieve an adsorption-desorption equilibrium, the mixture was magnetically stirred in the dark for 30 minutes before undergoing 90 minutes of irradiation for each experiment. The concentration of remaining OG dye in the supernatant solutions was measured using a UV-visible spectrophotometer based on the maximum absorption wavelength of OG dye at 482 nm. The mixed suspensions were tested at predetermined intervals and centrifuged to remove the photocatalyst. The following formula was used to evaluate the effectiveness of photodegradation [17-18].

$$\textbf{Percentage degradation} = \frac{C_0 - C}{C_0} \times 100 \quad \ldots\ldots\ldots\ldots \qquad (1)$$

Where C_0 is the concentration of OG dye before illumination, and C is the concentration after irradiation time.

2.6 Effect of pH on photocatalytic degradation of OG dye

To achieve the desired pH, the dye solution was prepared by usinga 0.1 M solution of either HCl or NaOH for adjusting the pH of the dye while continuously monitoring with a pH meter. The pH-adjusted solutions were then sonicated for 30 minutes to ensure uniformity of the solution. After sonication, the samples were exposed to visible light, and aliquots were taken at regular time intervals. The extent of photodegradation was assessed by measuring the absorbance using a UV-Vis spectrophotometer.

2.7 Antibacterial activity of Ag-MnO_2 NCs

The antibacterial activity of Ag-MnO_2 NCs was evaluated in vitro using the agar well diffusion method against Gram-positive bacteria (*Bacillus subtilis* and *Staphylococcus aureus*) and Gram-negative bacteria (*Pseudomonas aeruginosa* and *Escherichia coli*). Nanocomposite solutions were prepared at concentrations of 6, 12.5, 25, 50, 75, and 100 µg/mL using 0.5% dimethyl sulfoxide (DMSO) as the solvent. Nutrient agar plates were inoculated with the respective bacterial strains, and wells were formed and filled with either the nanocomposite solutions or streptomycin (30 µg/mL) as a positive control. The plates were incubated at 37 °C for 24 hours, after which the zones of inhibition were measured to assess antibacterial efficacy. Each experiment was conducted in triplicate, and results are presented as mean ± standard deviation.

3. RESULTS AND DISCUSSION

3.1 UV-visible analysis

The optical characteristics of manganese dioxide nanoparticles (MnO_2-NPs) and silver-doped manganese dioxide nanocomposites (Ag-MnO_2 NCs), such as band gap energy and absorption spectra, can be assessed using a key technique: UV-Visible spectroscopy. Figure 1(a) shows the absorbance spectrum of bio-synthesized MnO_2-NPs, which displays a peak at 348 nm. In contrast, the UV spectrum of Ag-MnO_2 NCs reveals a broad band at 426 nm. The calculated band gap energies for MnO_2-NPs and Ag-MnO_2 NCs are 2.58 eV and 1.96 eV, respectively, as determined from the extrapolation line depicted in Figures 1(b) and (d), which illustrate Tauc's plots for the biosynthesized nanomaterials. A significant shift in the absorption band was observed after incorporating silver nanoparticles into the MnO_2 layers. The addition of silver nanoparticles to the surface of MnO_2 is crucial as it enhances photocatalytic activity while remaining cost-effective [19].

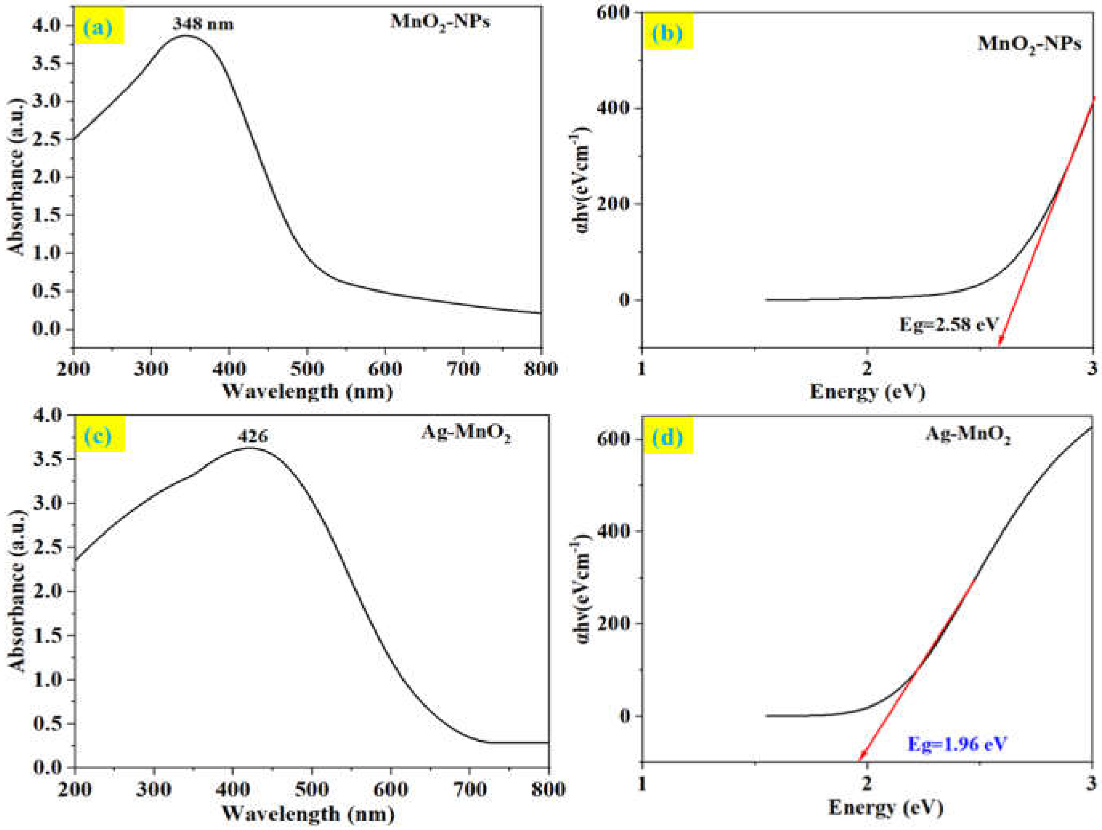

Fig. 1(a, c) UV–vis spectra of MnO_2-NPs and the Ag-MnO_2 NCs (**b, d**) Band gap energy of MnO_2-NPs and the Ag-MnO_2 NCs

3.2 XRD analysis

The XRD pattern for the biosynthesized Ag-MnO_2 NCs was characterized by specific diffraction angles (2θ) and corresponding peak intensities. Notable peaks were observed at 2θ values of 28.03˚, 33.65˚, 38.51˚, 44.15˚, 47.7˚, 56.95˚, 58.44˚, 63.17˚, and 74.28˚, which confirmed the hexagonal structure of the synthesized Ag-MnO2 nanocomposites. The significant diffraction planes were identified by their Miller indices (hkl) of (220), (310), (111), (200), (301), (411), (600), (220), and (311), as illustrated in Figure 2. This XRD pattern is consistent with the JCPDS file No. 89-3722. To determine the crystallite size of the resulting nanocomposite, we applied the Debye-Scherrer formula: $D = 0.9\lambda/\beta\cos\theta$. In this formula, β refers to the line broadening at half-maximum intensity (FWHM in radians on the 2θ scale), λ indicates the X-ray wavelength (1.5406 Å), θ is the Bragg angle, and D represents the crystallite size in nanometers. Utilizing the Scherer equation, we calculated the average particle size of the Ag-MnO_2 NCs to be 33.14 nm within the crystalline planes [20-21].

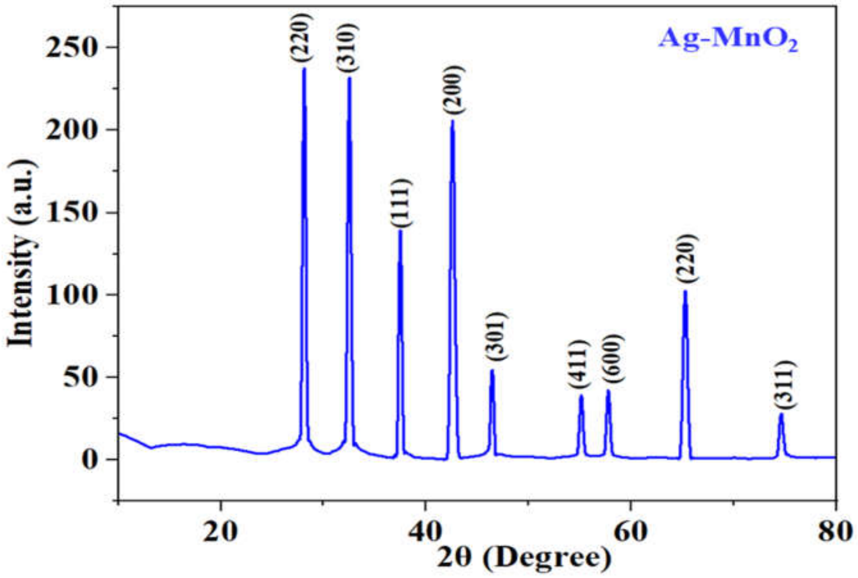

Fig. 2 XRD pattern of Ag-MnO$_2$ nanocomposites

3.3 FT-IR spectra analysis

The chemical bond vibrations of biosynthesized Ag-MnO$_2$ nanocomposites were examined using a FT-IR spectrometer. FT-IR spectra were recorded across both the high wavenumber and fingerprint regions, specifically from 4000 to 500 cm^{-1}. This analytical method employs infrared radiation to detect molecular vibrations, enabling the precise identification of functional groups and chemical structures [22]. The vibrational bands of the Ag-MnO$_2$ nanocomposites are illustrated in Figure 3, with notable peaks at 647, 1084, 1404, 1621, 2947, and 3340 cm^{-1}. Among these, the broad stretching vibration of the O-H group is represented by the band at 3340 cm^{-1}. The peaks observed at 1084, 1621, and 2947 cm^{-1} correspond to C-O-C, >C=O, and C-H stretching vibrations, respectively. A significant peak at 1404 cm^{-1} indicates the O-Mn-O stretching mode, which is associated with the bond between oxygen and manganese. Additionally, the peak at 647 cm^{-1} relates to the Mn-O lattice vibration, illustrating the dynamic interactions between manganese and oxygen within the lattice structure. This peak not only highlights the characteristics of the Mn-O bond environment but also provides valuable insights into the vibrational properties of the material, emphasizing the importance of these vibrational modes in understanding its structural and electronic behaviour [23].

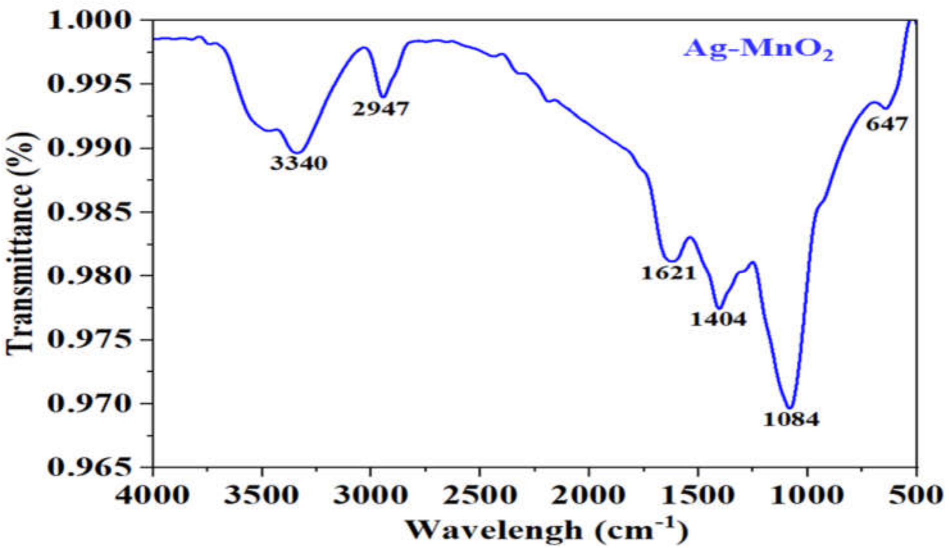

Fig. 3 FT-IR spectrum of Ag-MnO_2 nanocomposites

3.4 SEM and EDX analysis

The analysis of the SEM images offers valuable insights into the structure of the synthesized Ag-MnO_2NCs. In Figure 4a, the SEM image illustrates nearly spherical Ag-MnO_2nanoparticles that are well-distributed, although there are some indications of agglomeration. The elemental composition of the Ag-MnO_2NCs was analyzed using energy-dispersive X-ray spectroscopy (EDX), as illustrated in Fig. 4(b). Distinct peaks corresponding to carbon (C), oxygen (O), silver (Ag), and manganese (Mn) were observed in the EDX spectrum of Ag-MnO_2NCs.The expected elements within the Ag-MnO_2NCs were validated by the EDX spectrum shown in Figure 4b. This spectrum indicated the presence of silver (Ag, %), manganese (Mn, 20.2168.00%), oxygen (O, 3.3%), and carbon (C, 7.3%). Additionally, the lack of detectable traces of other elements in the EDX spectra corroborates the XRD data and confirms the purity of the synthesized product [24-25].

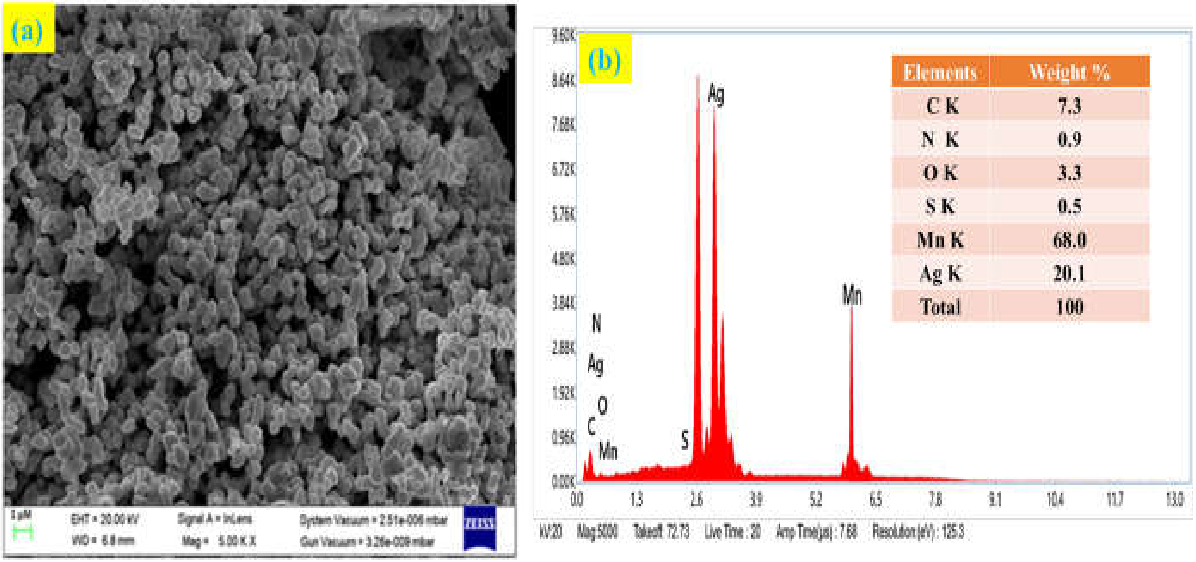

Elements	Weight %
C K	7.3
N K	0.9
O K	3.3
S K	0.5
Mn K	68.0
Ag K	20.1
Total	100

Fig. 4(a) SEM image of Ag-MnO_2 NCs and **(b)**EDX pattern of Ag-MnO_2 NCs

3.5 TEM analysis

Transmission electron microscopy (TEM) is widely employed in nanomaterial research as it enables direct visualization at the nanoscale, providing valuable information on morphology, crystallinity, and particle size distribution. HRTEM images(Fig. 5(a-d)) show spherical, triangular, and rectangular shapes of Ag-Mn Ag-MnO_2 nanoparticles at different magnifications. Fig. 5(e) shows the SAED pattern of synthesised Ag-MnO_2 NCs. SAED produces a diffraction pattern by concentrating an electron beam on a specific region; rings represent the material's crystal lattice planes. Fig. 5(f) illustrates the average particle size distribution curve, which yields an average particle size of 16.21 nm for Ag-MnO_2 NCs [26].

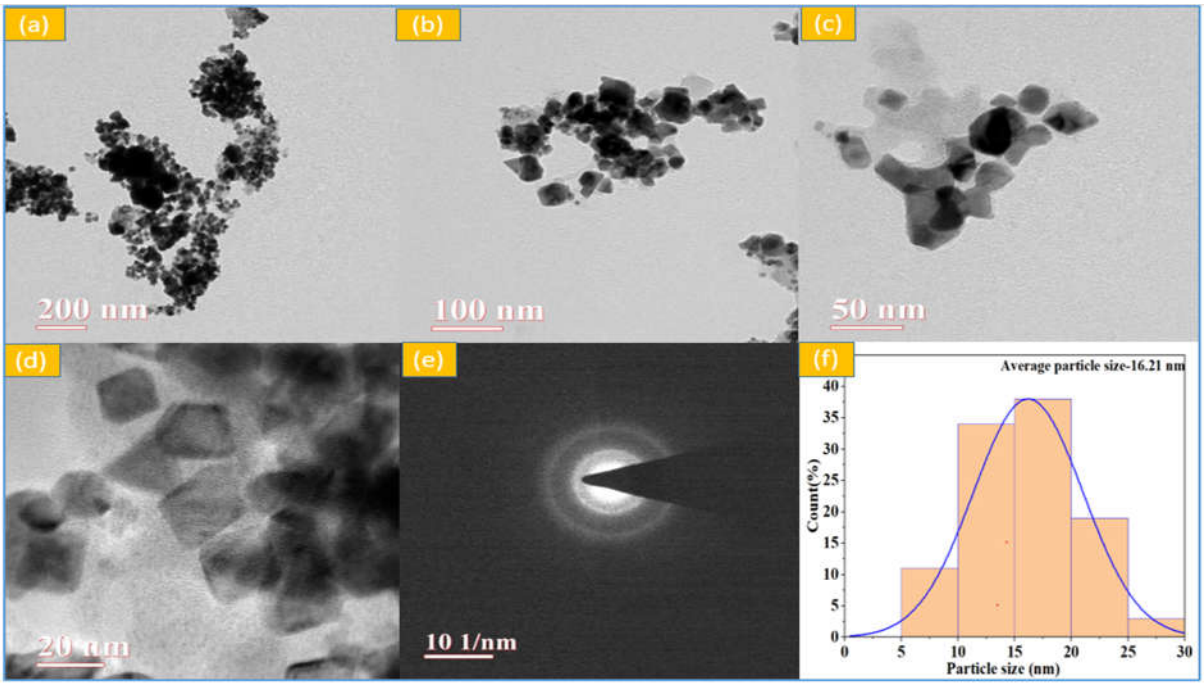

Fig. 5 (a-d) TEM images ofAg-MnO_2 NCs at different magnifications, **(e)** SAED pattern of Ag-MnO_2 NCs, **(f)** Average particle distribution curve of Ag-MnO_2 NCs

3.6 Assessments of photocatalytic dye degradation

The photocatalytic performance of MnO_2-NPs and Ag-MnO_2NCs was evaluated by examining the degradation of OG dye as a model reaction. The efficiency of photo degradation was assessed by monitoring the change in absorbance of the OG dye at 482 nm over various time intervals.

3.6.1 Effect of pH

The pH of the photocatalytic solution influences the photodegradation of OG dye, as illustrated in Fig. 6a. The pH of the solution affects the ionization state of dye molecules and the production of reactive oxygen species, which in turn influence the surface charge of the photocatalyst. The surfaces of most metal oxide photocatalysts typically become positively charged at lower pH values, which increases the adsorption of anionic dyes because of electrostatic attraction [27-28]. Experiments were performed with pH (2.0-12.0) for 100mL of 20 mg/L dye solution and the adsorbent dose of 60 mg. OG dye adsorption increases from 82% to 86% with an increase in pH (2.0-4.0); furthermore, there is no significant change at higher pH levels. At lower pH, the absorbent surface generates a net positive charge due to a higher concentration of H+ ions. As a result, there is an electrostatic repulsion between the OG dye molecules and the adsorbent surface, which inhibits OG dye removal. The maximum photodegradation of the OG dye is 92.6% at pH four and slightly decreases from 92.6% to 88.7% with increasing pH up to 12. Higher OH- ions generate a net negative charge on the adsorbent surface, which competes with OG dye ions. These results revealed that cationic and anionic dyes require a basic and acidic medium for maximum removal.

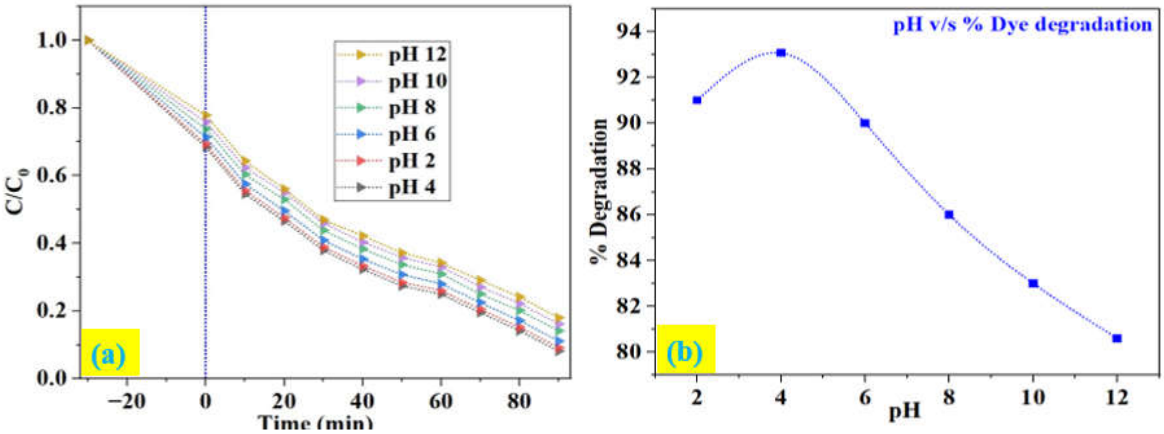

Fig. 6 (a, b) The influence of pH on photodegradation of OG dye by Ag-MnO_2 photocatalyst

3.6.2 Effect of dose

Figure 7 illustrates the effect of photocatalyst dosage on the degradation of Orange G (OG) dye. The amount of photocatalyst was varied from 20 to 100 mg, with a dye concentration of 20 mg/L at pH 4. The results showed that a dosage of 20 mg of photocatalyst achieved more than 64.0% degradation activity under visible light irradiation. Increasing the photocatalyst dosage to 100 mg improved the degradation of OG dye to 96.2%. This enhancement can be attributed to the increased surface area and the number of adsorption sites that come with a higher dosage of the adsorbent. These findings align with previous studies on the adsorption of OG dye [29].

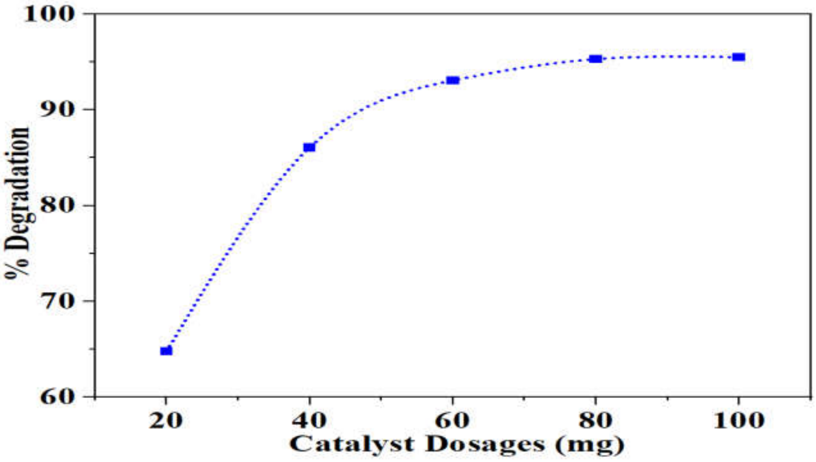

Fig. 7 Dosages of Ag-MnO_2photocatalyst on the photodegradation of OG dye

3.6.3 Effect of irradiation time

Light energy generates electron-hole pairs, making light intensity a crucial factor in the photocatalytic degradation of various dyes. When exposed to visible light, the photocatalyst can completely degrade Orange G

(OG) dye [30]. The effect of irradiation time on the degradation of OG dye was assessed using optimized concentrations of the photocatalysts, manganese dioxide nanoparticles (MnO_2-NPs) and silver-manganese dioxide nanocomposites (Ag-MnO_2 NCs), all under visible light exposure. The experimental results, presented in Figures 8a and 8b, demonstrate a consistent increase in dye removal efficiency with longer irradiation times for both photocatalysts.

Under optimized conditions (pH 4, 60 mg), the maximum degradation efficiencies of 65.48% and 91.90% were achieved after 90 minutes of irradiation for MnO_2-NPs and Ag-MnO_2NCs photocatalysts, respectively. Following this duration, the degradation rate reached a flats, indicating a saturation point.

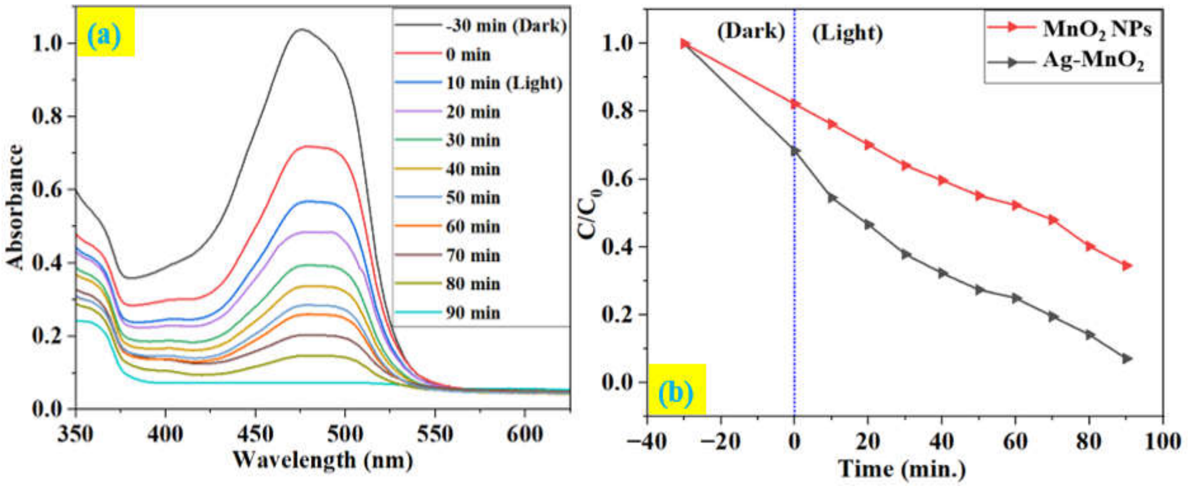

Fig. 8 (a) Time-dependent UV–Vis absorption spectra of the Photodegradation of OG dye in the presence of Ag-MnO_2 NCs **(b)** The effect of OG dye degradation by MnO_2 NPsand Ag-MnO_2 NCs

3.7 Kinetics of dye reaction

Time dependence investigations were carried out to track the development of the photocatalytic reaction. The experimental data fit well with the pseudo-first-order kinetic model, suggesting that the rate of degradation is primarily dependent on the initial concentration of the dye. The aliquots of the sample were taken out at regular intervals, and the absorbance's were measured to track the progress of the reaction. The percentage of degradation is plotted against time under visible light irradiation [31]. The kinetic analysis was evaluated using the pseudo-first-order equation:

$$-\ln (Ct/Co) = kt \qquad \ldots\ldots\ldots\ldots\ldots(2)$$

where C_o is the starting dye concentration, C_t is the dye concentration at time t, and k is the reaction rate constant. The pseudo-first-order rate constant (k) of the reaction was calculated from the plot of -ln (C_o/C_t) vs. time, as shown in Fig. 9 (a). The results show that the Ag-MnO_2 NCs exhibit a significantly higher reaction rate compared to MnO_2-NPs. The degradation rate constant (k) demonstrated an increase with the doping of silver, achieving a peak value of 0.01932 min-1, in contrast to the rate of 0.00849 min-1 observed for MnO_2-NPs (Fig. 9b). The corresponding values for the rate constant, degradation efficiency, and regression coefficient (R2) for Ag-MnO_2-NCs and MnO_2-NPs are 0.9765 and 0.9575, respectively. The Ag-MnO_2 NCs demonstrated the highest rate constant (k), indicating their superior photocatalytic efficiency for the degradation of OG dye. This demonstrates that the produced photocatalyst efficiently breaks down the OG dye molecule when exposed to visible light.

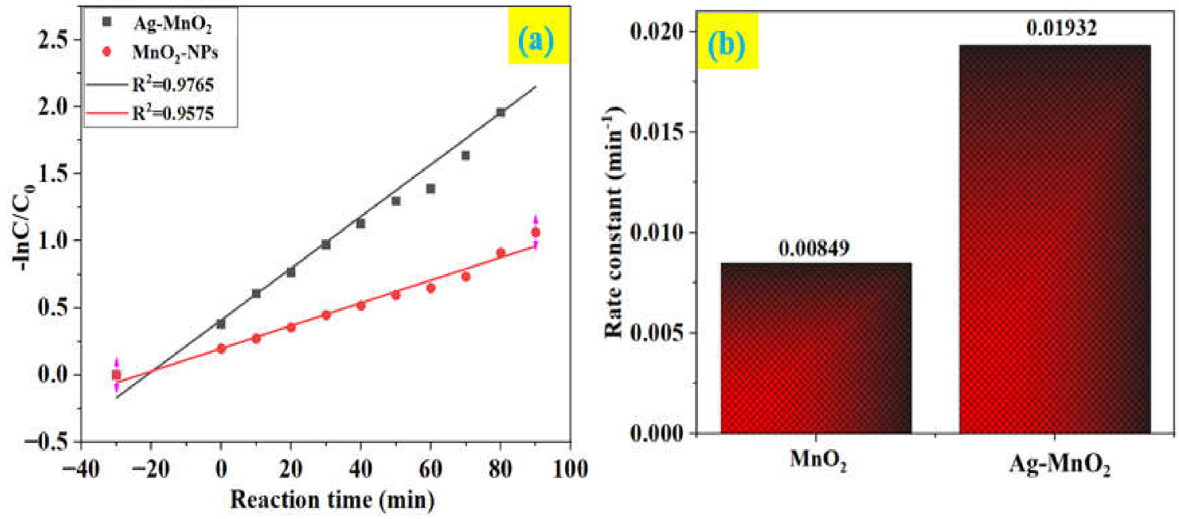

Fig. 9(a) The plot of OG dye degradation byAg-MnO$_2$ NCs and MnO$_2$-NPs (-ln (C_t /C_0) *vs.* reaction time), and (**b**) bar diagram for rate constants for OG dye degradation by Ag-MnO$_2$ NCs and MnO$_2$-NPs

3.8 Photodegradation mechanism of OG dye

The photocatalytic reaction generally deals with surface oxidation-reduction processes, charge separation and migration, and photoexcitation. The mechanism of dye photodegradation has been studied using a variety of methods, including the addition of scavengers to solutions to remove reactive species like h^+, •OH and •O_2^- and the detection of intermediates using a variety of previously described techniques [32]. The photodegradation mechanism of OG dye by Ag-MnO$_2$ NCs shows in the presence of light. The Ag-MnO$_2$ NCs absorb photons and generate electron–hole pairs. The photogenerated electrons (e^-) can migrate to the surface and reduce adsorbed oxygen (O_2) molecules, resulting in the formation of hydrogen peroxide (H_2O_2). In the presence of photoinduced holes (h^+), H_2O_2further decomposes to yield reactive superoxide radicals (•O_2^-). Simultaneously, the holes (h^+) in the valence band of Ag-MnO$_2$ NCs have sufficient oxidative potential to react with surface hydroxide ions (OH^-), producing highly reactive hydroxyl radicals (•OH). These reactive oxygen species (•O_2^- and •OH), along with the holes, act synergistically to degrade OG dye molecules. The end products of this photocatalytic degradation process are carbon dioxide (CO_2), water (H_2O), and other benign byproducts. The all steps of photodegradation of OG dye was given as follows:

$$\begin{aligned}
\text{Ag-MnO}_2\ \text{NCs} + h\nu &\longrightarrow h^{+} + e^{-}\\
H_2O &\longrightarrow H^{+} + OH^{-}\\
h^{+} + OH^{-} &\longrightarrow {}^{\cdot}OH\\
O_2 + e^{-} &\longrightarrow {}^{\cdot}O_2^{-}\\
{}^{\cdot}O_2^{-} + H^{+} &\longrightarrow HO_2^{\cdot}\\
2HO_2^{\cdot} &\longrightarrow O_2 + H_2O_2\\
H_2O_2 + e^{-} &\longrightarrow {}^{\cdot}OH + {}^{-}OH\\
H_2O_2 + O_2 &\longrightarrow {}^{\cdot}OH + {}^{-}OH + O_2\\
{}^{\cdot}O_2^{-}/\,{}^{\cdot}OH + \text{OG Dye} &\longrightarrow \text{Degrade + Product}
\end{aligned}$$

3.9 Reusability

The reusability studies on the Ag-MnO2 NCs photocatalyst under visible light irradiation were conducted for the degradation of OG dye. As seen in Fig. 10, the photocatalyst was utilised to break down a 60 mg/100 mL solution of OG. The progress of the reaction was tracked by measuring the absorbance of aliquots of the reaction solution taken at regular intervals. The degradation percentages for the five cycles were 91.90 % to 86.9% for visible light irradiation, representing a decrease of approximately 5% compared to the initial cycle performance. According to the results, the catalyst maintains its initial efficiency almost unchanged even after five cycles of reuse when exposed to visible light. This demonstrates the economic viability of the photocatalytic dye degradation technique. Table 1 illustrated the comparison of efficiencies of reported photocatalysts for photodegradation of OG dye.

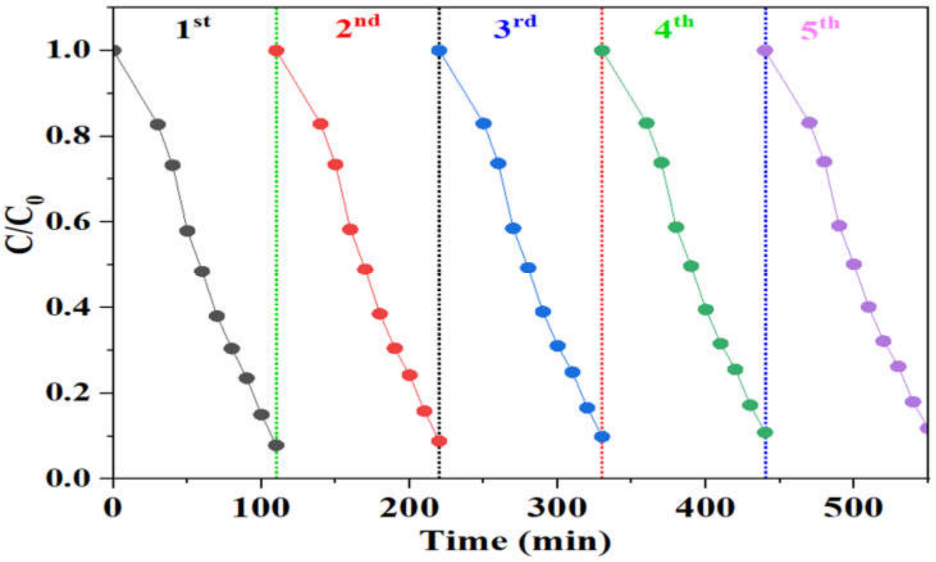

Fig. 10 The degradation of OG dye molecules using Ag-MnO$_2$ photocatalyst under visible light irradiation.

Table 1: Comparison of efficiencies of photocatalysts used for degradation studies of OG dye

S. No.	Adsorbent	Dosage (g/L)	Concentration (mg/L)	Capability (mg/g)	Ref.
1.	ZnO-AC	0.02	50	153.8	33
2.	α-Fe_2O_3	0.05	50	62.0	34
3.	$CoFe_2O_4$	0.05	50	52.3	34
4.	Co_3O_4	0.05	50	33.3	34
5.	MgO	0.05	-	19.3	35
6.	Uncalcined Mg-Fe-CO_3	1.0	200	76.4	36
7.	Calcined Mg-Fe-CO_3	1.0	200	378.8	36
8.	Activated carbon	0.02	400	293.15	37
9.	Chitosan	0.02	400	1270.71	37
10.	Hematite (α-Fe_2O_3)	1.0	25	0.63	38
11.	Fe_3O_4/MIL-101(Cr)	0.03	50	200.0	39

3.10 Antibacterial activity

The in vitro antibacterial activity of six distinct doses of Ag-MnO_2 NCs (6.25, 12.5, 25, 50, 75, and 100 µgmL^{-1}) against certain pathogens including *B. subtilis*, *S. aureus*, *E. coli*, and *P. aeruginosa* was evaluated,using the agar well diffusion method. The inhibitory zones are presented in Fig. 11 and Tables 2. The highest concentration of Ag-MnO_2 NCs showed the greatest growth inhibition was 100µg mL^{-1}, as demonstrated by the growth inhibition of *E. coli* (19 mm), *B. subtilis* (21 mm), *P. aeruginosa* (21 mm), and *S. aureus* (19 mm). The bio-synthesised Ag-MnO_2 NCs showed strong antibacterial activity against the human diseases they were intended to target. *B. subtilis* and *P. aeruginosa*have the biggest inhibitory zones, measuring 21.03 mm, followed by *E. coli*, which had the inhibitory zones equal to 19.17 mm, and *S. aureus*, which had the lowestinhibitory zones, measuring 19.03 mm, according to the data. Overall, our findings showed that the antibacterial qualities of bio-synthesised compounds may be impacted by the presence of potent bioactive components. According to the findings, Ag-MnO_2 NCs are highly effective against human pathogens, which results in their capacity to inhibit bacterial growth. The antibacterial activity of nanomaterials is primarily dependent on their size and concentration, and it is more noticeable against Gramme negative than Gramme positive pathogens [40]. For every pathogen, the growth of inhibition was confirmed and documented. The comparative study of these pathogens is given in the Fig. 12.

Table 2: Antibacterial activity of Ag-MnO_2 NCs and zone of inhibition in mm (Results are displayed as mean ± SD)

Bacterial Strains	^{a}**Diameter of Zone of Inhibition (mm) for Ag-MnO_2NCs** ^{b}**Diameter of Zone of Inhibition (mm) for Streptomycin**					
	Concentration in µg/mL					
	6.25	**12.5**	**25**	**50**	**75**	**100**
B. subtilis	7.63 ± 0.65^{a} 34.03±0.35^{b}	8.03 ±0.35^{a} 35.07±0.4^{b}	9.07±0.6^{a} 36.03±0.25^{b}	10.13±0.42^{a} 37.07±0.35^{b}	14.03±0.35^{a} 38.07±0.4^{b}	21.03±0.45^{a} 39.07±0.31^{b}
S. aureus	8.03 ±0.15^{a} 30.03± 0.35^{b}	11.07± 0.21^{a} 31.03±0.25^{b}	12.1±0.46^{a} 32.03±0.25^{b}	15.03±0.45^{a} 33.03±0.35^{b}	17.03±0.55^{a} 35.03±0.35^{b}	19.03±0.45^{a} 36.03±0.35^{b}
E. Coli	9.03±0.25^{a} 29.00±0.4^{b}	10.03± 0.25^{a} 30.03±0.35^{b}	11.03± 0.15^{a} 31.12±0.34^{b}	14.1±0.36^{a} 32.13±0.42^{b}	18.01±0.41^{a} 33.08±0.53^{b}	19.17± 0.47^{a} 35.16±0.56^{b}
P. aeruginosa	0.00± 0.00^{a} 33.07±0.31^{b}	0.00±0.00^{a} 35.03±0.25^{b}	7.10±0.46^{a} 37.07±0.21^{b}	9.06±0.34^{a} 38.1±0.56^{b}	14.09±0.41^{a} 39.04±0.4^{b}	21.03±0.47^{a} 40.06±0.51^{b}

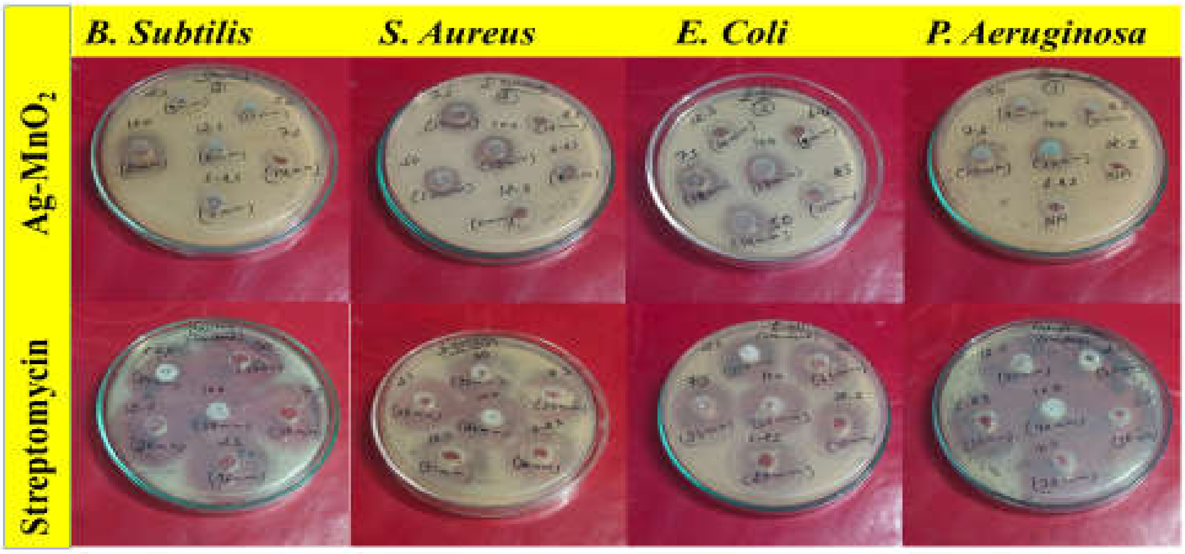

Fig. 11: The antibacterial efficacy of Ag-MnO_2NCsat different concentrations and streptomycin was measured against selected pathogenic bacterial strains

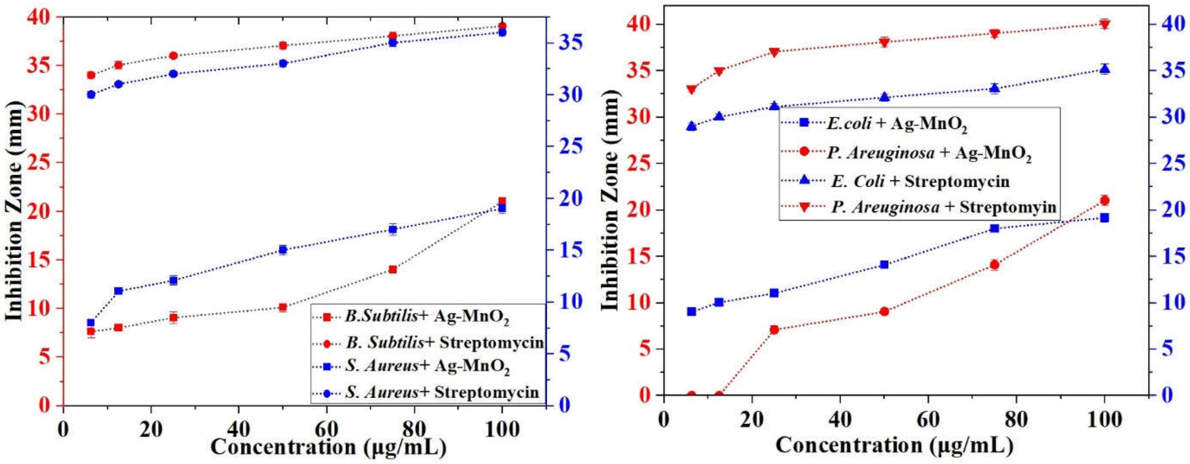

Fig. 12: The comparative antibacterial activity of the Ag-MnO_2 NCs was assessed against both (**a**) gram-positive and (**b**) gram-negative bacterial strains

4. Conclusion

This study successfully utilized *Lawsonia inermis* leaf extract for the green synthesis of silver-doped manganese oxide nanocomposites (Ag–MnO_2 NCs). The synthesized nanocomposites underwent comprehensive characterization through various physicochemical techniques, which confirmed a uniform dispersion of silver nanoparticles across the manganese dioxide layers, with an average particle size of approximately 16.21 nm, as determined by transmission electron microscopy (TEM)

analysis. Ultraviolet-visible (UV–Vis) absorption spectra indicated an enhanced absorption of visible light by Ag–MnO_2 NCs when compared to pristine manganese dioxide. The findings revealed that photocatalytic activity was significantly influenced by factors such as catalyst dosage, dye concentration, and the solution's pH. Under optimal conditions (20 mg/L Orange G at 4 pH levels), approximately 92% of the dye was degraded within a 90-minute timeframe. Kinetic analysis revealed that the degradation process followed pseudo-first-order kinetics, with an apparent rate constant of 0.01932 min^{-1}. Additionally, the Ag–MnO_2 NCs exhibited commendable stability in aqueous environments, underscoring their potential as effective and environmentally friendly photocatalysts for wastewater treatment applications.The Ag–MnO_2 NCs exhibited pronounced antibacterial activity against both Gram-positive (Bacillus subtilis, Staphylococcus aureus) and Gram-negative (Escherichia coli, Pseudomonas aeruginosa) bacterial strains. These results highlight the promise of the green-synthesized nanocomposite as a cost-effective and multifunctional material, offering potential applications as both an efficient photocatalyst and a chemotherapeutic alternative.

Acknowledgments

We would like to express our gratitude to the Department of Chemistry, University of Rajasthan, Jaipur and MNIT, Jaipur for providing essential infrastructure and facilities. We also thank Dr. Chitra Jain from Biomitra Life Sciences Pvt. Ltd. for their generous assistance during the in vitro antibacterial experiments.

Conflict of Interests

The authors declare they have no competing financial interests or personal relationships that could influence the work reported in this paper.

Data Availability Statement

Data will be made available on request.

5. References

1. P. Gregory, “Dyes and dye intermediates,” *Kirk-Othmer Encyclopedia of Chemical Technology*, pp. 1–66, 2000.
2. S. Mandal and J. Venkatramani, “A review of plant-based natural dyes in leather application with a special focus on color fastness characteristics,” *Environ. Sci. Pollut. Res.*, vol. 30, no. 17, pp. 48769–48777, 2023.
3. M. T. Islam, T. Islam, T. Islam, and M. R. Repon, “Synthetic dyes for textile colouration: Process, factors and environmental impact,” *Text. Leather Rev.*, vol. 5, pp. 327–373, 2022.
4. T. A. Khattab, M. S. Abdelrahman, and M. Rehan, “Textile dyeing industry: Environmental impacts and remediation,” *Environ. Sci. Pollut. Res.*, vol. 27, no. 4, pp. 3803–3818, 2020.
5. T. Islam, M. R. Repon, T. Islam, Z. Sarwar, and M. M. Rahman, “Impact of textile dyes on health and ecosystem: A review of structure, causes, and potential solutions,” *Environ. Sci. Pollut. Res.*, vol. 30, no. 4, pp. 9207–9242, 2023.
6. A. K. Samanta and A. Konar, “Dyeing of textiles with natural dyes,” *Natural Dyes*, vol. 3, no. 30–56, pp. 212–222, 2011.
7. K. D. Djebbar, “Removal of an azo dye (Orange G) by various methods in homogeneous phase: Comparative study,” *Jordan J. Chem.*, vol. 6, no. 3, pp. 307–319, 2011.
8. H. Sonia, S. Kumari, S. Chahal, S. Devi, S. Kumar, and A. Kumar, “Spinel ferrites/metal oxide nanocomposites for wastewater treatment,” *Appl. Phys. A*, vol. 129, no. 2, p. 91, 2023.
9. X. Zhang, P. Wei, D. Sun, Z. Ni, J. Dou, B. Li, and B. Hu, “Hydrothermal syntheses and structural characterizations of polyoxometalate (Mo/W) compounds consisting of ML cations (M = Mn, Co, Ni, Cu, Zn; L = 3-(2-pyridyl) pyrazole),” *Cryst. Growth Des.*, vol. 9, no. 10, pp. 4424–4428, 2009.
10. R. Yang, Y. Fan, R. Ye, Y. Tang, X. Cao, Z. Yin, and Z. Zeng, “MnO_2-based materials for environmental applications,” *Adv. Mater.*, vol. 33, no. 9, p. 2004862, 2021.
11. N. S. Devi, P. Rekha, C. P. Lorena, V. S. Patricia, A. H. María, R. R. Devi, and S. Thanikaikarasan, “Silver doped manganese dioxide as an efficient photocatalyst for solar light induced degradation of malachite green dye and antibacterial activity,” *Int. J. Adv. Sci. Eng.*, vol. 2, pp. 4069–4086, 2024.
12. M. Harun-Ur-Rashid, T. Foyez, S. B. N. Krishna, S. Poda, and A. B. Imran, “Recent advances of silver nanoparticle-based polymer nanocomposites for biomedical applications,” *RSC Adv.*, vol. 15, no. 11, pp. 8480–8505, 2025.

13. B. Ajitha, Y. A. K. Reddy, P. S. Reddy, Y. Suneetha, H. J. Jeon, and C. W. Ahn, “Instant biosynthesis of silver nanoparticles using *Lawsonia inermis* leaf extract: Innate catalytic, antimicrobial and antioxidant activities,” *J. Mol. Liq.*, vol. 219, pp. 474–481, 2016.
14. B. Malaikozhundan, S. Mohandoss, R. Krishnamoorthi, P. V. Bharathi, S. Palanisamy, and J. Vinodhini, “Enhanced bactericidal, antibiofilm and antioxidative response of *Lawsonia inermis* leaf extract synthesized ZnO NPs loaded with commercial antibiotic,” *Bioproc. Biosyst. Eng.*, vol. 47, no. 8, pp. 1241–1257, 2024.
15. C. Krishnaraj, B. J. Ji, S. L. Harper, and S. I. Yun, “Plant extract-mediated biogenic synthesis of silver, manganese dioxide, silver-doped manganese dioxide nanoparticles and their antibacterial activity against food- and water-borne pathogens,” *Bioproc. Biosyst. Eng.*, vol. 39, no. 5, pp. 759–772, 2016.
16. N. S. Devi, P. Rekha, C. P. Lorena, V. S. Patricia, A. H. María, R. R. Devi, and S. Thanikaikarasan, “Silver doped manganese dioxide as an efficient photocatalyst for solar light induced degradation of malachite green dye and antibacterial activity,” *Int. J. Adv. Sci. Eng.*, vol. 2, pp. 4069–4086, 2024.
17. X. An, S. Erramilli, and B. M. Reinhard, “Plasmonic nano-antimicrobials: properties, mechanisms and applications in microbe inactivation and sensing,” *Nanoscale*, vol. 13, no. 6, pp. 3374–3411, 2021.
18. R. Messai, M. F. Ferhat, B. Belmekki, M. W. Alam, M. A. S. Al-Othoum, and S. Sadaf, “GAD plasma-assisted synthesis of ZnO nanoparticles and their photocatalytic activity,” *Mater. Res. Express*, vol. 11, no. 1, p. 015006, 2024.
19. B. Sachdeva, K. Aggarwal, A. Singh, K. Kumari, R. Chandra, and S. Singh, “Advancements in silver-based nanocatalysts for organic transformations and other applications: A comprehensive review (2019–2024),” *RSC Adv.*, vol. 15, no. 22, pp. 17591–17634, 2025.
20. V. J. Mane, S. B. Kale, S. B. Ubale, V. C. Lokhande, and C. D. Lokhande, “Enhanced specific energy of silver-doped MnO_2/graphene oxide electrodes as facile fabrication symmetric supercapacitor device,” *Mater. Today Chem.*, vol. 20, p. 100473, 2021.
21. V. Kumar, P. Saharan, A. K. Sharma, A. Umar, I. Kaushal, A. Mittal, and B. Rashad, “Silver doped manganese oxide-carbon nanotube nanocomposite for enhanced dye-sequestration: Isotherm studies and RSM modelling approach,” *Ceram. Int.*, vol. 46, no. 8, pp. 10309–10319, 2020.
22. L. Chellappan, B. Thangaraj, N. Muthukurumban, and V. Gurusamy, “Investigations on chemically synthesized pure and doped manganese dioxide nanoparticles for dye removal and photocatalytic applications,” *J. Fluoresc.*, vol. 35, no. 3, pp. 1549–1564, 2025.

23. M. E. Assal, M. R. Shaik, M. Kuniyil, M. Khan, J. V. Kumar, A. Y. Alzahrani, and S. F. Adil, “Silver-doped manganese based nanocomposites for aerial oxidation of alcohols,” *Mater. Express*, vol. 8, no. 1, pp. 35–54, 2018.
24. S. A. Alzahrani, S. A. Al-Thabaiti, W. S. Al-Arjan, M. A. Malik, and Z. Khan, “Preparation of ultra-long α-MnO_2 and Ag@MnO_2 nanoparticles by seedless approach and their photocatalytic performance,” *J. Mol. Struct.*, vol. 1137, pp. 495–505, 2017.
25. M. S. Elshikh, I. Abid, C. O. Asadu, E. O. Umeagukwu, T. W. Chen, E. V. Belekbaevna, and Z. A. Toktoralievna, “Sustainable utilization of oak bark for MnO_2 catalyst synthesis,” *Catal. Lett.*, vol. 154, no. 11, pp. 5941–5947, 2024.
26. C. Bharti, A. Singh, K. Nandan, and S. Baghel, “Antibacterial and cytotoxic efficacy of Ag–MnO_2/PIn nanocomposites derived from battery waste,” *Mater. Chem. Phys.*, vol. 333, p. 130305, 2025.
27. S. Banerjee, M. C. Chattopadhyaya, and Y. C. Sharma, “Removal of an azo dye (Orange G) from aqueous solution using modified sawdust,” *J. Water Sanit. Hyg. Dev.*, vol. 5, no. 2, pp. 235–243, 2015.
28. Y. Y. Maruo, K. Akaoka, and J. Nakamura, “Development and performance evaluation of ozone detection paper using azo dye Orange I: Effect of pH,” *Sens. Actuators B Chem.*, vol. 143, no. 2, pp. 487–493, 2010.
29. M. Q. Cai, X. Q. Wei, Z. J. Song, and M. C. Jin, “Decolorization of azo dye Orange G by aluminum powder enhanced by ultrasonic irradiation,” *Ultrason. Sonochem.*, vol. 22, pp. 167–173, 2015.
30. K. D. Djebbar, “Removal of an azo dye (Orange G) by various methods in homogeneous phase: Comparative study,” *Jordan J. Chem.*, vol. 6, no. 3, pp. 307–319, 2011.
31. M. Asgher and H. N. Bhatti, “Mechanistic and kinetic evaluation of biosorption of reactive azo dyes by free, immobilized and chemically treated *Citrus sinensis* waste biomass,” *Ecol. Eng.*, vol. 36, no. 12, pp. 1660–1665, 2010.
32. M. Saeed, M. Muneer, A. U. Haq, and N. Akram, “Photocatalysis: An effective tool for photodegradation of dyes—a review,” *Environ. Sci. Pollut. Res.*, vol. 29, no. 1, pp. 293–311, 2022.
33. J. Saini, V. K. Garg, R. K. Gupta, and N. Kataria, “Removal of Orange G and Rhodamine B dyes from aqueous system using hydrothermally synthesized zinc oxide loaded activated carbon (ZnO-AC),” *J. Environ. Chem. Eng.*, vol. 5, no. 1, pp. 884–892, 2017.
34. M. Y. Nassar, T. Y. Mohamed, I. S. Ahmed, N. M. Mohamed, and M. Khatab, “Hydrothermally synthesized Co_3O_4, α-Fe_2O_3, and $CoFe_2O_4$ nanostructures: Efficient nano-adsorbents for the

removal of Orange G textile dye from aqueous media," *J. Inorg. Organomet. Polym. Mater.*, vol. 27, no. 5, pp. 1526–1537, 2017.

35. M. Y. Nassar, T. Y. Mohamed, I. S. Ahmed, and I. Samir, "MgO nanostructure via a sol–gel combustion synthesis method using different fuels: An efficient nano-adsorbent for the removal of some anionic textile dyes," *J. Mol. Liq.*, vol. 225, pp. 730–740, 2017.
36. N. B. H. Abdelkader, A. Bentouami, Z. Derriche, N. Bettahar, and L. C. De Menorval, "Synthesis and characterization of Mg–Fe layer double hydroxides and its application on adsorption of Orange G from aqueous solution," *Chem. Eng. J.*, vol. 169, no. 1–3, pp. 231–238, 2011.
37. S. Imam, A. I. Muhammad, H. F. Babamale, and Z. U. Zango, "Removal of Orange G dye from aqueous solution by adsorption: A short review," *J. Environ. Treat. Tech.*, vol. 9, no. 1, pp. 318–327, 2021.
38. M. K. Mondal, S. Singh, M. Umareddy, and B. Dasgupta, "Removal of Orange G from aqueous solution by hematite: Isotherm and mass transfer studies," *Korean J. Chem. Eng.*, vol. 27, no. 6, pp. 1811–1815, 2010.
39. T. Wang, P. Zhao, N. Lu, H. Chen, C. Zhang, and X. Hou, "Facile fabrication of Fe_3O_4/MIL-101 (Cr) for effective removal of acid red 1 and Orange G from aqueous solution," *Chem. Eng. J.*, vol. 295, pp. 403–413, 2016.
40. R. K. Kunkalekar, M. M. Naik, S. K. Dubey, and A. V. Salker, "Antibacterial activity of silver-doped manganese dioxide nanoparticles on multidrug-resistant bacteria," *J. Chem. Technol. Biotechnol.*, vol. 88, no. 5, pp. 873–877, 2013.